Real-time *in situ* determination of inductively coupled power and numerical prediction of power distribution in RF ion thrusters

IEPC-2017-161

Presented at the 35th International Electric Propulsion Conference
Georgia Institute of Technology – Atlanta, Georgia – USA
October 8–12, 2017

C. Volkmar*, A. Neumann†, C. Geile‡ and K. Hannemann§
German Aerospace Center, Institute of Aerodynamics and Flow Technology, Spacecraft Department,
Bunsenstrasse 10, 37073 Goettingen, Germany

Abstract: We show a systematical approach to obtain the forwarded electrical power to sustain the plasma discharge in radio-frequency ion thrusters using a commercial current and voltage sensor system. With knowledge of the power directly at the coil, a numerical model delivers the power-to-thrust-ratio as well as the distribution of power into several channels of loss, including collisions and structural eddy currents. With this work, we are, furthermore, able to distinguish between two phenomena that affect the power-to-thrust-ratio – one caused by the physics of the plasma itself and the other caused by the mismatch of the impedance bridge spanned between the electrical load of the thruster and the driving generator.

I. Introduction

Electric propulsion assemblies are constituted by the actual thruster and several peripheral devices supplying it with propellant, power and operational signaling. Performance optimization strategies are, therefore, ideally conducted on the assembly level which shifts the historically rather scientific view on those thrusters to a systems engineering one. With this translation comes a phenomenon not often mentioned in literature: the interaction of the thruster with its power electronics.

With this work, we want to introduce an approach that helps to better understand the interaction of radio-frequency ion thrusters (RIT) with their radio-frequency generators (RFG). The RFG is a crucial part of a RIT assembly but there is only few information available that studies the impact of the two systems on each other. In our approach, we want to emphasize that this device has a significant influence on the overall power balance of a RIT assembly.

Radio-frequency generators used in RIT assemblies are typically composed of a half-bridge topology which is operated in near-resonant mode around.[6] The thruster itself is composed of an induction coil which is typically wrapped around a cylindrical, trapezoidal or hemispherical discharge chamber. Additionally, a set of either two or three extraction grids is attached to the discharge vessel and used for electrostatic ion extraction. More details can exemplarily be found in.[7,8]

A basic propulsive system assembly covers the thruster and the Power Supply and Control Unit (PSCU) which is subdivided into the RFG, a DC power supply for the RFG, a mass flow controller (MFC) and DC power supplies for positive and negative voltages (PHV, NHV) for the extraction grid system. The RFG is attached to the coil of the thruster using a coaxial or triaxial feeding cable. In this configuration, the thruster is driven within a resonant circuit consisting of the inductance of the thruster L_{RIT}, an equivalent

*Electric Propulsion Research Engineer, chris.volkmar@dlr.de
†Head of Electric Propulsion Facility, a.neumann@dlr.de.
‡Electric Propulsion Technician, christopher.geile@dlr.de
§Head of Spacecraft Department, klaus.hannemann@dlr.de

ohmic resistance R_{RIT} that includes plasma, coil wire and eddy current losses and a series capacitance C_{res} that is part of the output stage of the RFG. The control logic of the RFG is based on a phase-locked-loop/frequency-locked-loop (PLL/FLL) scheme that tends to switch one of the transistors when the current measured in the return line is near zero. This method is referred to as zero-current-switching and is used to efficiently transfer power to a load if the source has small output resistance.[9] This methodology is known as impedance bridging and enables transfer efficiency greater 0.5. In contrast to impedance matching, which is commonly used in 50 Ω–RF systems with $\eta \approx 0.5$, it is possible to overcome severe power loss within the generator in bridging mode.[10]

Since the load of the above-defined resonant circuit is defined by the plasma parameters it comprises a highly dynamic behavior if the thruster is driven in different operational modes, e.g. transition from low- to high-thrust mode. Depending on the relation R_{RIT}/R, with R denoting the output resistance of the generator including the RF cable, the efficiency of power coupling will somehow be affected which ultimately leads to power loss in the generator/cable. Since most scientists and engineers only refer to the power drawn from the DC supply P_{DC}, they might get misled when assessing performance data of the thrusters such as the power-to-thrust-ratio (PTTR).

Here, we want to differentiate between the DC power and the actual RF power that is forwarded to the thruster to sustain the plasma discharge at given points of operation by means of phase-resolved power measurement. The experimental setup and the methodology are shown in Sec. III in more detail. The accurate power measurement was achieved by an Impedans Poly Octiv *VI* sensor which is available commercially. This device has the advantage of low insertion loss and thus hardly any impact on the resonant circuit itself. Preceding attempts such as shown in[11] always suffered from unstable latency and phase shift between voltage and current sensors and hence exhibited large error bars, if the experiments were not conducted in thermal equilibrium. It is evident that this is not always possible due to different processes like mode transitions or even the diurnal thermal cycle.

With the experimentally acquired RF power, a direct statement about coupling efficiency is possible with

$$\eta = \frac{P_{\mathrm{RF}}}{P_{\mathrm{DC}}}. \tag{1}$$

The remaining power $(1-\eta)\,P_{\mathrm{DC}}$ is lost within the generator and feeding cable and can currently not be divided any further. However, since the semi-conductor junction resistance is commonly known from data sheets an approximate relation of the losses may be deduced from that. Here, however, we will instead focus on the power transferred to the thruster with aid of numerical modeling. With this model which is explained in more detail in Sec. II we can furthermore divide P_{RF} into several channels of loss. Those are typically wire and eddy current loss, ionization and excitation loss, wall flux and sheath potential loss as well as elastic, Coulomb and stochastic collision loss. With this methodology it is, therefore, possible to exactly reveal the power distribution of the complete assembly which is considered very valuable for optimizing system performance and creating input parameters for thermal analyses which additionally aim to increase the system quality.

II. Model Overview

A flow chart of the model developed is shown in Fig. 1. In the following, the model is introduced, covering its working principle, basic assumptions used and the most important features for the actual study. The model's complete architecture and other detailed information can be found in.[12,13]

The assumptions made within the proposed model correspond to those used within the vast majority of volume-averaged models[14–20] which mostly follow Lee and Lieberman's approach—at least to a certain extent—published in.[21]

The self-consistent flow starts with the input of the axi-symmetric geometry of the thruster consisting of discharge chamber, extraction grid system, thruster housing and other conducting parts within the assembly. In axi-symmetric systems $\partial/\partial\phi = 0$ holds true, with ϕ denoting the azimuthal component.

The loop depicted in Fig. 1 is started with the solution of a charge conservation equation that relates the volume ionization rate to the loss of charge to the walls:

$$K_{\mathrm{iz}} n_{\mathrm{n}} = \frac{u_{\mathrm{B}}}{d_{\mathrm{eff}}} \tag{2}$$

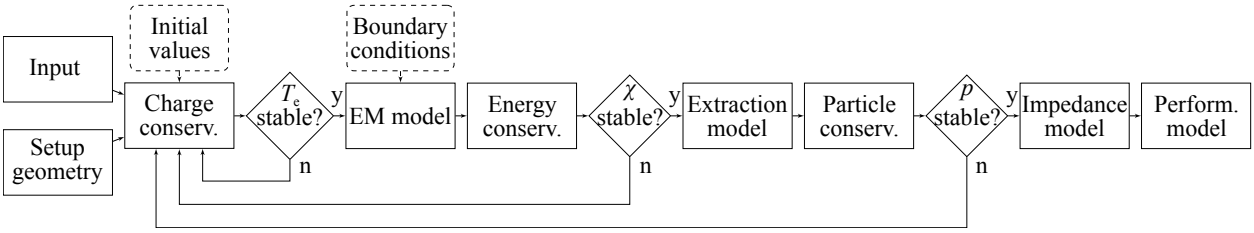

Figure 1. Flow chart of the numerical model. It consists of three conservation equations (charge, energy and mass conservation) that are iteratively brought to convergence. The variables solved for are the volume-averaged electron temperature T_e, the ionization fraction $\chi = n_e/(n_e + n_n)$, with n_e and n_n denoting electron density and neutral particle density, respectively, and the discharge pressure p. To account for geometric aspects of the thruster as well as eddy current losses, an axi-symmetric electromagnetic model is used.

In this equation, K_{iz} denotes the Maxwellian-averaged rate constant for ionization and d_{eff} the effective plasma bulk size which is iteratively calculated with an analytic expression for the plasma sheath thickness. After convergence, the mean Maxwellian electron temperature can be derived analytically. The cross sections for the collisions are taken from.[22,23]

The second equation that is solved is an energy conservation equation. Energy conservation is achieved if the deposited electromagnetic power in the plasma, which is calculated by the electromagnetic model, equals the power lost to collisions:

$$\frac{1}{2}\iiint_V \left|\widetilde{\mathbf{E}}\right|^2 \operatorname{Re}\kappa_p \,\mathrm{d}V = P_{coll} \tag{3}$$

Here, $\widetilde{\mathbf{E}}$ denotes the induced electric field. The link between plasma and electromagnetic model is given by the conductivity κ_p which again is determined by the plasma parameters:

$$\kappa_p \approx \frac{\epsilon_0 \omega_{pe}^2}{\nu_{en,eff}^2 + \omega_{eff}^2}\left(\nu_{en,eff} - \mathrm{i}\omega_{eff}\right) \tag{4}$$

In this equation, ϵ_0 denotes the vacuum permittivity, ω_{pe} the electron plasma frequency; i.e, the collective response of electrons to the excitation by electric fields, $\nu_{en,eff}$ the effective electron-neutral collision frequency which is given by $\nu_{en,eff} = \nu_{en} + \nu_{ei} + \nu_{stoc}$ and ω_{eff} the effective radio-frequency the electrons are oscillating with. This effective frequency slightly differs from the applied RF due to the kinetic processes the distribution function of electrons causes. It is calculated following an approach shown in.[24]

The governing equation for the electromagnetic model is the time-harmonic quasi-stationary diffusion equation:[25]

$$\nabla \times \left(\frac{1}{\mu}\nabla \times \widetilde{\mathbf{A}}\right) + \mathrm{i}\omega\kappa\widetilde{\mathbf{A}} + \widetilde{\mathbf{J}}_s = \mathbf{0} \tag{5}$$

This is assumed valid for RITs because the wavelength of the applied current signal through the coil is typically orders of magnitude larger than the coil wire. Therefore, radiation will only play a minor role. In this equation, $\widetilde{\mathbf{A}}$ denotes the phasor of the vector potential field, $\widetilde{\mathbf{J}}_s$ denotes the phasor of the source current density field and $\mu = \mu_0\mu_r$ the permeability, with the vacuum permeability μ_0 and the relative permeability μ_r, of the media within the simulation domain. In the axi-symmetric representation, only the azimuthal component of the vector potential field is of interest, leading to $\widetilde{\mathbf{A}} = \widetilde{A}_\phi \mathbf{u}_\phi$, with $\mathbf{u}_\phi$ denoting the unit vector in azimuthal direction. The conductivity is defined per Eq. (4) in plasma regions. Conductivities of metallic structures are also implemented as a function of material and temperature. The conductivity is assumed to be isotropic, no magnetic confinement is modeled.

The solver for the vector potential is based on a Finite-Difference representation of Eq. (5) which is not further explained in this paper. Since the pre-sheath region is not modeled, there is no scalar potential distribution—which in reality builds up due to ambi-polar diffusion. Hence, the electric, magnetic and induced current density fields are directly derived from the diffusion equation as suggested by literature.[25]

With the axi-symmetric representation high resolution in the $r - z$ plane is achievable. Features like the impact of the skin and proximity effect in the coil wire can thus be taken into account while the model can still be run on a standard desktop computer.

In order to have the elecromagnetic model calculate the correct deposited power density within the plasma a realistic representation of the plasma density distribution—which ultimately determines the distribution of conductivity—is modeled using heuristic profiles introduced and verified in.[26] The distribution H follows a parabolic shape defined by

$$H = \sqrt{\left[1 - \left(\sqrt{1-h_r^2}\,\frac{r}{r_0}\right)^2\right]\left[1 - \left(\sqrt{1-h_z^2}\,\frac{z}{z_0}\right)^2\right]}, \tag{6}$$

with h_r and h_z denoting the density bulk-to-sheath-edge ratios.[21] Those ratios highly depend on the discharge parameters T_e and p and are, therefore, iteratively calculated as well.

With the deposited power Eq. (3) can be solved for n_e until convergence of the ionization fraction $\chi = n_\mathrm{e}/\left(n_\mathrm{e} + n_\mathrm{n}\right)$, which closes the second loop depicted in Fig. 1.

The next conservation equation to be solved is a particle balance that relates the amount of particles leaving the thruster through the extraction grid to the amount of particle inflow through the inlet nozzle. The particles leaving the thruster are either ions or atoms. The thrust producing ion flux is commonly expressed as a beam current which calculates to

$$I_\mathrm{b} = e h_\mathrm{grid} n_\mathrm{e} u_\mathrm{B} A_\mathrm{grid} \alpha_\mathrm{i}, \tag{7}$$

with $h_\mathrm{grid} n_\mathrm{e}$ being the charge carrier density at the grid boundary of the simulation domain, A_grid the grid area and α_i the transparency of the extraction grid system for ions.[27] Since α_i is not known a priori and since no particle tracking code is used, an additional loop not shown in Fig. 1 starts with a guess and the parameter is iteratively updated until the deposited power matches the experimentally obtained power measured within the resonant circuit. This methodology is validated by the Child-Langmuir law which predicts the *maximum* achievable current in case of unlimited plasma yield.

To close the loop, the amount of neutral gas leaving the thruster γ_n is also calculated as shown in.[12,13] This allows for determination of the mass utilization efficiency

$$\eta_\mathrm{m} = \frac{I_\mathrm{b}}{I_\mathrm{b} + e\gamma_\mathrm{n}}. \tag{8}$$

After convergence of the conservation equations, the self-consistent loop is finished and physical meaningful results are obtained. From those converged parameters, the thruster impedance can be derived. The Poynting theorem for time-harmonic fields, neglecting the radiative term due to large wavelength compared to the coil's size, is used to evaluate the lumped circuit elements' values that are used to describe the discharge on a technical layer:[25]

$$\frac{1}{2}\widetilde{I}^*\widetilde{V} = \frac{1}{2}\iiint_V \left|\widetilde{\mathbf{E}}\right|^2 \kappa_\mathrm{p}\,\mathrm{d}V + 2\mathrm{i}\omega \iiint_V \left(u_\mathrm{e} - u_\mathrm{m}\right)\,\mathrm{d}V \tag{9}$$

In this equation, the asterisk denotes the conjugate-complex of a quantity and u_e as well as u_m denote electric and magnetic energy density, respectively. Those energy densities can be derived from the electromagnetic fields defined earlier. The resistive and reactive components of the load impedance can be derived from Eq. (9).

Furthermore, the propulsive performance of the thruster such as thrust and specific impulse can be derived from the converged solution. Taking the mean kinetic velocity of neutrals $\overline{v}_\mathrm{n}$ and the electrostatically accelerated velocity of ions $v_\mathrm{i} = \left(2eV_\mathrm{scr}/m_\mathrm{i}\right)^{1/2}$ and their respective fluxes leaving the thruster into account and assuming $m_\mathrm{i} \approx m_\mathrm{n}$, the total thrust is obtained:

$$T = m_\mathrm{i}\left(\gamma_\mathrm{i} v_\mathrm{i} + \gamma_\mathrm{n}\overline{v}_\mathrm{n}\right) \tag{10}$$

The specific impulse can finally be calculated to

$$I_\mathrm{sp} = \frac{v_\mathrm{eff}}{g_0}, \tag{11}$$

with the effective exhaust velocity $v_\mathrm{eff} = T/m_\mathrm{i}\left(\gamma_\mathrm{i} + \gamma_\mathrm{n}\right)$ and standard gravity g_0.[15]

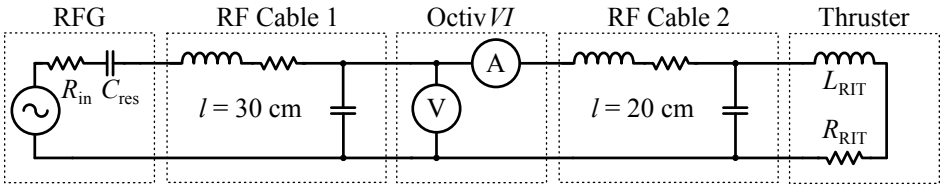

Figure 2. Schematic diagram of the experimental setup. Input and load impedance are slightly altered due to parasitic RF cable impedance. Due to short cable length and thus $R_{RIT} > R_{in} \gg R_{cable}$, the influence is neglected for the calculation of power distribution.

III. Experiment

The experimental setup for *in-situ* power measurement is schematically shown in Fig. 2. An Octiv *VI* probe from Impedans Ltd is used. Due to its patented spectrum-averaging methodology[28] it offers high phase-stability and nominal resolution down to 0.01°. It furthermore offers phase-resolved voltage and current measurement up to several hundred MHz and exhibits hardly no insertion loss (manufacturer's definition: 0.1 dB) into the circuit under test. For verification, a test without the probe was performed prior to the power measurement. No change in thruster performance; i.e., DC power consumption, was observed which verifies the nominal data of the probe.

The coaxial feeding cables slightly change source and load impedance, respectively. However, due to short cable lengths, this effect is assumed negligible for the assessment of power distribution. The reactance of the RG 213 cables used in this setup is essentially of inductive type since the load is typically driven at around 2 MHz. Hence, $1/\omega C \gg \omega L$, with C denoting the cables' capacitance which is in the order of some $\mathrm{pF\,m^{-1}}$ and L denoting their inductance in the order of $100\,\mathrm{nH\,m^{-1}}$. Based on that, there is substantially no current driven through the capacitive shunt. Additionally, ohmic losses are in the order of several $\mathrm{m\Omega\,m^{-1}}$ and thus no significant power consumption of the cables is expected.

Once the RFG has matched the load by tuning its frequency to the resonant frequency

$$\omega_0 = \frac{1}{\sqrt{(L + L_{\mathrm{RIT}})\, C_{\mathrm{res}}}} \tag{12}$$

the reactances cancel each other leaving only the ohmic components R_{in} and R_{RIT}. The relation of those resistances determines the power forwarded to the thruster and thus the plasma discharge. The signals within the resonant circuit are continuously captured using the Octiv *VI* probe. Due to the characteristics of the resonant circuit, the current and the voltage signals' values are amplified with respect to the DC inputs' values. From those signals, all the important quantities like impedance, coupled power and coupling efficiency are derived.

IV. Results

Two different sets of input parameters are investigated here. The parameter sets—or modes—are defined by the screen grid voltage V_{scr}, the acceleration grid voltage V_{acc} and the ion beam current I_{b}. Within both modes the acceleration grid current I_{acc} was well below 1 % of the screen grid current I_{scr} leading to $I_{\mathrm{b}} = I_{\mathrm{scr}} - I_{\mathrm{acc}} \approx I_{\mathrm{scr}}$. The modes of thruster operation are shown in Tab. 1.

Both, simulation and experiment were performed with those modes. In mode 1, the neutral xenon volumetric inflow rate was varied from $\dot{V} = 1 \ldots 10\,\mathrm{sccm}$. Due to instabilities at higher mass flow, the inflow rate in mode 2 was limited to $\dot{V} = 1 \ldots 8\,\mathrm{sccm}$.

The thruster used for this work is a RIT-10/37 engine developed by the University of Giessen and

Table 1. Thruster modes for numerical and experimental investigation.

	V_{scr}	V_{acc}	I_{b}
Mode 1:	1800 V	−300 V	9.97 mA
Mode 2:	1800 V	−300 V	15.25 mA

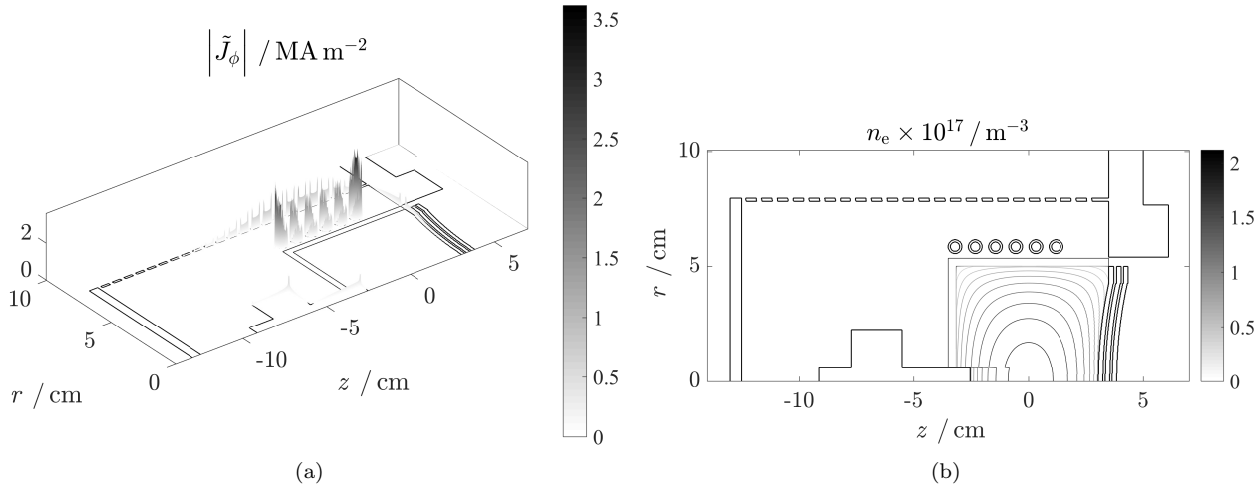

Figure 3. Current density inside the structural components of the thruster (a). The plasma charge current density for $\dot{V} = 1\,\mathrm{sccm}$ in mode 1 according to Eq. (6) is shown in (b).

distributed by TransMIT GmbH. It is composed of a discharge chamber with 10 cm in diameter and an extraction system with 37 beamlets. The nominal thrust level of this thruster lies in the lower single-digit mN range.

In the following, some numerically obtained results are shown to give an overview of the plasma parameters as well as the performance of the thruster.

An important physical effect that is determinable with aid of the model is the proximity effect in the coil wire which is depicted in terms of the current density inside the conductive structures in Fig. 3 (a). This effect is caused by the current density inside adjacent coil windings. The magnetic fields caused by those currents compensate each other between the windings and hence displace the current density to regions of low nominal opposing field strengths. This effect, in contrast to the well-understood skin effect, is hardly impossible to account for analytically since it is a strong function of geometry. A very realistic current distribution—which again influences the coupling of energy from coil to plasma—can be derived with this functionality. It is thus considered extremely valuable to account for the proximity effect in RIT simulations.

The charge carrier density distribution, as depicted in Fig. 3 (b), follows the parabolic profile defined in Eq. (6). The parameters shaping the profile are being solved self-consistently. The density corresponds to $\dot{V} = 1\,\mathrm{sccm}$ in mode 1.

Thrust and specific impulse of modes 1 and 2 are shown in Fig. 4 (a) and (b), respectively. A parallelogram-like thrust balance manufactured by Advanced Space Technologies GmbH was used to measure the thrust in one nominal working point ($\dot{V} = 3\,\mathrm{sccm}$ in mode 2). It shows large error bars in the lower mN range since it has been designed for higher thrust levels up to 250 mN.[29] It is here only used to perform a plausibility check of the model.

Figure 4 (a) shows the ion thrust for modes 1 and 2 which is held constant by the parameters defined in Tab. 1. Furthermore, the impact of the neutral gas leaving the thruster can be determined with aid of the self-consistent model. The curves show that especially in areas of low thrust, as is the case with the RIT-10/37, there is a significant contribution of neutrals to the overall delivered thrust. The influence of the neutral gas flow is also depicted in Fig. 4 (b) in terms of I_{sp}. The thruster under test comprises only few extraction apertures and is hence not optimized for high I_{sp} applications which is typically the case for RITs. However, even using this non-ideal grid system $I_{\mathrm{sp}} \approx 2000\,\mathrm{s}$ may be achieved by tuning $\dot{V} < 1\,\mathrm{sccm}$. Unfortunately, the mass flow controller used for this study showed unstable behavior in this range and could not be used to record further data points.

Figure 5 shows the coil currents for modes 1 and 2. The error bars are due to measurement inaccuracy of the grid current data acquisition which is based on a 10 bit AD converter. The resolution of the positive high voltage (PHV) voltage supply attached to the screen grid is 0.59 mA which manifests in fairly high uncertainty when going down to low beam currents. With $P_{\mathrm{DC}}, P_{\mathrm{RF}} \propto I_{\mathrm{scr}}$ it follows that

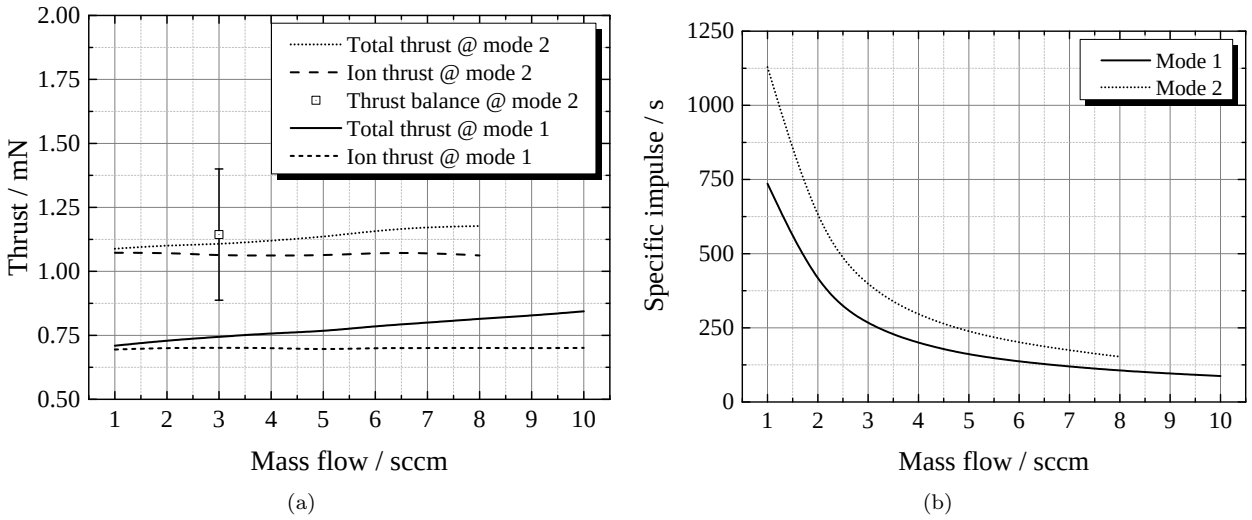

Figure 4. Thrust (a) and specific impulse (b) of the RIT-10/37 thruster in operation modes 1 and 2.

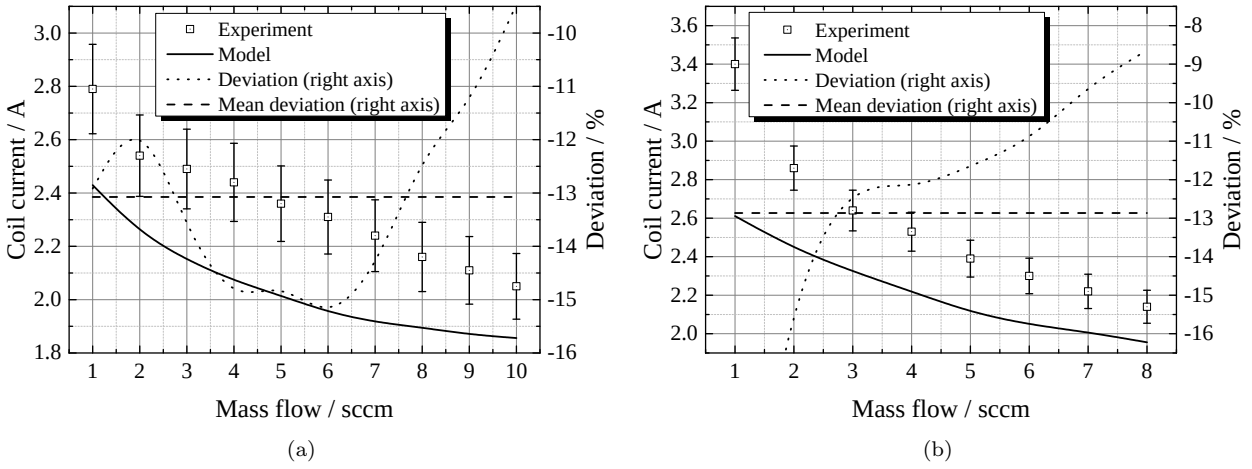

Figure 5. Experimentally and numerically obtained coil currents for modes 1 (a) and 2 (b). The mean deviation of the model is about 13 % below the measured values.

$\Delta P_{\mathrm{DC}}, \Delta P_{\mathrm{RF}} \propto \Delta I_{\mathrm{scr}}$, with Δ being the absolute error. This error estimation is directly applicable to the coil current with $\Delta I_{\mathrm{RF}} = \left(\Delta P_{\mathrm{RF}}/R_{\mathrm{RIT}}\right)^{1/2}$.

There is an observable deviation between the coil currents calculated by the model and the measured values which is mainly due to the plasma discharge being described using continuum methods. This claim is supported by the development of the deviation (dashed lines in Fig. 5 (a) and (b)) which approaches smaller values when going to higher flow rates. The Knudsen numbers $\mathrm{Kn} = \lambda/l$, with the mean free path between collisions λ and the characteristic length scale l along which collisions take place, evaluates the rarefication of gas particles within the discharge. For the working points presented here they lie between absolutely rarefied ($\mathrm{Kn} \geq 10$) and approaching continuum ($\mathrm{Kn} < 0.1$). This area is also referred to as transition regime. Given the simplicity of the proposed model and thus the short simulation duration of only a few minutes per data point the deviation is acceptable. More accurate results could be obtained by using a free molecular kinetic type of code like Direct Simulation Monte Carlo (DSMC).[32]This would imply long simulation times and is thus not the scope of this work because simulation duration is considered a crucial aspect for engineering purposes.

The power distribution within the thruster including structural losses is depicted in Fig. 6 (a). It is observable that a significant amount of power is lost to excitation processes, especially when going to higher

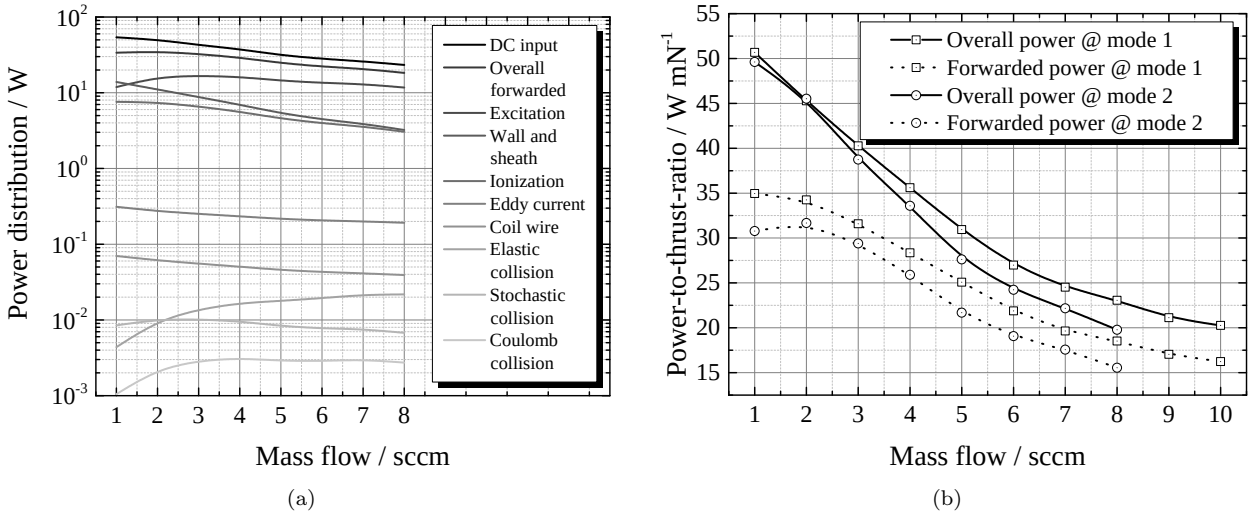

Figure 6. Power distribution for mode 2 (a). With aid of this functionality, the model can be used to determine the channels of loss which offers the opportunity of optimizing the thruster at a very detailed level. Power-to-thrust-ratio (PTTR) (b). The decrease of PTTR at low flow rates is attributed to the mismatch of the impedance bridge representing by the coupling efficiency.

mass flows. This behavior is expected due to increasing pressure inside the discharge chamber and hence decreasing mean free length between collisions. At very low pressure, as indicated in the figure below 2 sccm, the electron energy is high enough to rather ionize a particle instead of exciting it to a higher energy state because electrons gain a lot of energy from the accelerating electric field due to very large mean free length between collisions. This is also observed in the experiment. The discharge appears darker at lower flow rates. Since the extracted amount of ions is kept constant the consequence is that there is less excitation and hence less radiative transitions. For further information the cross sections of the corresponding processes should be assessed.[22]

It is furthermore expected that eddy current losses inside the thruster might be higher in reality. Since the geometric representation is merely an approximation of the actual thruster some features like screws, sharp edges and other irregularities are not considered at the moment. In a next release, the model will be updated to be capable of importing CAD drawings which is anticipated to describe structural losses more realistically.

The numerically obtained thrust from Fig. 4 (a) together with the measured forwarded and DC power is used to introduce the power-to-thrust-ratio (PTTR) in Fig. 6 (b). It can be seen that the PTTR in case of DC power increases to lower mass flows. In contrast to that the PTTR of the actual forwarded power decreases in areas of low mass flow. This is due to the aforementioned mismatch of the impedance bridge between RFG and thruster. The mismatch is caused by decreasing thruster resistance which can be derived from the measured phase-resolved voltage and current signals. This decrease leads to an electrically adverse relation between source and load resistance which again results in power loss within the generator.

V. Conclusion

We presented a concise approach based on experimental and numerical studies to distinguish between power absorption at assembly and thruster level. The power consumption of the assembly, prominently consisting of the thruster, the RFG and feeding cables, has to be interpreted with great care due to effects like impedance bridge mismatch. Power lost to this channel is often attributed to effects inside the thruster—or the plasma—and thus may open room for miscalculation of actual thruster performance. An applicable example is given by the PTTR. We showed that especially in areas of low mass flow, which are prominently aspired in space missions due to longevity, there is a difference of about $30 - 40\,\%$ between DC input and forwarded RF power. This information can furthermore be used for thermal modeling of the assembly.

The model used in this work is based on a continuum approach of the plasma discharge. It is considered

adequate because the sources of error are well understood and the error itself lies in acceptable areas. The identified errors are reported and discussed and appropriate solution approaches are suggested. A major advantage of the model is its simulation time which is on the scale of minutes per working point. Because of that, the model can be used as a virtual prototype which is considered beneficial for optimization strategies during thruster development.

The experimental setup was based on a phase resolved voltage and current meter as well as the thruster assembly including all the necessary peripherals. Due to low resolution of the extracted ion current measurement there is a non-negligible error. This is an unfortunate fact that will be assessed by high resolution AD converters and/or an optimized extraction grid that allows for more ion current to be extracted. The latter requires a RFG that is capable of power levels up to several hundred watts which is currently under development.

The presented hybrid approach consisting of power measurement and post-processed simulation offers a detailed insight into the plasma physics within the inductive discharge. With this methodology, the integral telemetry data during measurement can be matched to actual processes inside the discharge. We believe that this methodology is crucial for efficient optimization of RIT assemblies. Furthermore, we clearly showed the necessity of power measurement directly at the inductive load, as mentioned earlier in terms of PTTR. Optimization of energy coupling from coil to plasma is deemed drastically improved by following this proposed methodology.

References

[1]Killinger, R., Kukies, R., Surauer, M., Tomasetto A., and van Holtz, L., "ARTEMIS Orbit Raising Inflight Experience with Ion Propulsion", *Acta Astronautica*, Vol. 53, 2003, pp. 607-621.

[2]Martinez-Sanchez, M. and Pollard, J. E., "Spacecraft Electric Propulsion–An Overview", *Journal of Propulsion and Power*, Vol. 14, No. 5, 1998, pp. 688-699.

[3]Rayman, M. D. and Williams, S. N., "Design of the First Interplanetary Solar Electric Propulsion Mission", *Journal of Spacecraft and Rockets*, Vol. 39, No. 4, 2002, pp. 589-595.

[4]Mazouffre, S., "Electric Propulsion for Satellites and Spacecraft: Established Technologies and Novel Approaches", *Plasma Sources Science and Technology*, Vol. 25, No. 3, 2016, Article 033002.

[5]Hutchins, M., Simpson, H. and Jimenez, J. P., "QinetiQ's T6 and T5 Ion Thruster Electric Propulsion System Architectures and Performances", *Proceedings of the 34th International Electric Propulsion Conference*, Hyogo-Kobe, Japan, 2015, Proceeding IEPC-2015-131.

[6]Simon, J., Probst, U. and Klar, P. J., "Development of a Radio-Frequency Generator for RF Ion Thrusters", *Transactions of the Japan Society for Aeronautical and Space Sciences, Aerospace Technology*, Vol. 14, No. ists30, 2016, Article Pb_33.

[7]Leiter, H. J, Loeb, H. W. and Schartner, K.-H., "The RIT-15 Ion Engines–A Survey of the Present State of Radio Frequency Ion Thruster Technology and its Future Potentiality", *Third International Conference on Spacecraft Propulsion*, Cannes, France, 2000, pp. 423-432.

[8]Bassner, H., Killinger, R., Leiter, H. and Mueller, J., "Development Steps of the RF-Ion Thrusters RIT", *Proceedings of the 27th International Electric Propulsion Conference*, Passadena, USA, 2001, Proceeding IEPC-2001-105.

[9]Erickson, R. W. and Maksimovic, D., *Fundamentals of Power Electronics*, 2nd ed., Springer US, New York City, USA, 2001.

[10]Bowick, C., Blyler, J. and Ajluni, C., *RF Circuit Design*, 2nd ed., Newnes, Philadelphia, USA, 2007.

[11]Simon, J., Volkmar, C. and Probst, U., "High-Precision Power Measurement for Accurate Characterization of RF Ion Thrusters", *Proceedings of the 5th International Conference on Space Propulsion*, Rome, Italy, 2016, Proceeding SP2016_3124614.

[12]Volkmar, C. and Ricklefs, U., "Implementation and Verification of a Hybrid Performance and Impedance Model of Gridded Radio-Frequency Ion Thrusters", *European Physical Journal D*, Vol. 69, 2015, Article 227.

[13]Volkmar, C., Ricklefs, U. and Klar, P. J., "Self-Consistent Numerical 0D/3D Hybrid Modeling of Radio-Frequency Ion Thrusters", *Transactions of the Japan Society for Aeronautical and Space Sciences, Aerospace Technology*, Vol. 14, No. ists30, 2016, Article Pb_23.

[14]Lieberman, M. A. and Lichtenberg, A. J., *Principles of Plasma Discharges and Materials Processing*, 2nd ed., Wiley, New Jersey, USA, 2005.

[15]Goebel, D. M. and Katz, I., *Fundamentals of Electric Propulsion: Ion and Hall Thrusters*, 1st ed., Wiley, New Jersey, USA, 2008.

[16]Chabert, P. and Braithwaite, N. S. J., *Physics of Radio-Frequency Plasmas*, 1st ed., Cambridge University Press, New York, USA, 2011.

[17]Goebel, D. M., "Analytical Discharge Model for RF Ion Thrusters", *IEEE Transactions on Plasma Science*, Vol. 36, 2008, pp. 2111-2121.

[18]Chabert, P., Monreal, J. A., Bredin, J., Popelier, L. and Aanesland, A., "Global Model of a Gridded-Ion Thruster Powered by a Radiofrequency Inductive Coil", *Physics of Plasmas*, Vol. 19, 2012, Article 073512.

[19]Tsay, M. M. and Martinez-Sanchez, M., "Simple Performance Modeling of a Radio-Frequency Ion Thruster", *Proceedings of the 30th International Electric Propulsion Conference*, Florence, Italy, 2007, Proceeding IEPC-2007-072.

[20]Turkoz, E. and Celik, M., "2-D Electromagnetic and Fluid Models for Inductively Coupled Plasma for RF Ion Thruster Performance Evaluation", *IEEE Transactions on Plasma Science*, Vol. 42, 2014, pp. 235-240.

[21]Lee, C. and Lieberman, M. A., "Global Model of Ar, O2, Cl2, and Ar/O2 Highdensity Plasma Discharges", *Journal of Vacuum Science and Technology A*, Vol. 13, 1995, pp. 368-380.

[22]Hayashi, M., "Bibliography of Electron and Photon Cross Sections with Atoms and Molecules Published in the 20th Century– Xenon–", NIFS, NIFS-DATA-79, 2003.

[23]Hayashi, M., "Determination of Electron-Xenon Total Excitation Cross-Sections, from Threshold to 100 eV, from Experimental Values of Townsend's α", *Journal of Physics D: Applied Physics*, Vol. 16, 1983, pp. 581-589.

[24]Godyak, V. A., Piejak, R. B. and Alexandrovich, B. M., "Electron Energy Distribution Function Measurements and Plasma Parameters in Inductively Coupled Argon Plasma", *Plasma Sources Science and Technology*, Vol. 11, 2002, pp. 525-543.

[25]Jackson, J. D., *Classical Electrodynamics*, 3rd ed., Wiley, New Jersey, USA, 1998.

[26]Dobkevicius, M. and Feili, D., "A Coupled Performance and Thermal Model for Radio-Frequency Gridded Ion Thrusters", *European Physical Journal D*, Vol. 70, 2016, Article 227.

[27]Farnell, C. C., "Performance and Lifetime Simulation of Ion Thruster Optics", PhD Dissertation, Colorado State University, USA, 2007.

[28]Scullin, P. and Hopkins, M., "Analysing RF Signals from a Plasma System", Patent WO 2014016357 A3, 2014.

[29]Neumann, A., "STG-ET: DLR Electric Propulsion Test Facility", *Journal of Large-Scale Research Facilities JLSRF*, Vol. 3, 2017, Article A108.

[30]Neumann, A., "Update on Diagnostics for DLR's Electric Propulsion Test Facility", *Procedia Engineering*, Vol. 185, 2017, pp. 47-52.

[31]Dankanich, J. W., Walker, M., Swiatek, M. W. and Yim, J. T., "Recommended Practice for Pressure Measurement and Calculation of Effective Pumping Speed in Electric Propulsion Testing", *Journal of Propulsion and Power*, Vol. 33, No. 3, 2017, pp. 668-680.

[32]Bird, G. A., *Molecular Gas Dynamics and the Direct Simulation of Gas Flows*, 2nd ed., Clarendon Press, Oxford, UK, 1994.